

Preflight Spectral Calibration of the Orbiting Carbon Observatory

Jason O. Day, Christopher W. O'Dell, Randy Pollock, Carol J. Bruegge, David Rider, David Crisp, and Charles E. Miller

Abstract—We report on the preflight spectral calibration of the first Orbiting Carbon Observatory (OCO) instrument. In particular, the instrument line shape (ILS) function as well as spectral position was determined experimentally for all OCO channels. Initial determination of these characteristics was conducted through laser-based spectroscopic measurements. The resulting spectral calibration was validated by comparing solar spectra recorded simultaneously by the OCO flight instrument and a collocated high-resolution Fourier transform spectrometer (FTS). The spectral calibration was refined by optimizing parameters of the ILS as well as the dispersion relationship, which determines spectral position, to yield the best agreement between these two measurements. The resulting ILS profiles showed agreement between the spectra recorded by the spectrometers and FTS to approximately 0.2% rms, satisfying the preflight spectral calibration accuracy requirement of better than 0.25% rms.

Index Terms—Carbon dioxide (CO₂), instrument line shape (ILS), Orbiting Carbon Observatory (OCO), spectral calibration.

I. INTRODUCTION

THE Orbiting Carbon Observatory (OCO) was a National Aeronautics and Space Administration (NASA) Earth System Science Pathfinder (ESSP) mission designed to measure global column CO₂ concentrations twice a month with the precision and accuracy required to detect sources and sinks on regional scales [1]–[3]. It was launched on February 24, 2009, but did not achieve orbit due to a failure of the launch vehicle. However, the details of its preflight calibration are relevant both in their own right and as a guide for the calibration of the OCO-2 instrument, planned for launch in February 2013.

This paper describes the prelaunch spectral calibration of the OCO instrument, determined during thermal vacuum testing of the instrument at the Jet Propulsion Laboratory (JPL) in early 2008. The radiometric calibration of OCO is described in a companion paper [4]. The spectral calibration includes two

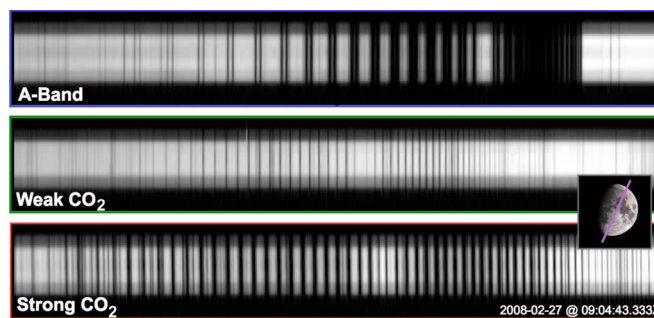


Fig. 1. Single frame of data (0.3-s exposure) from (top) the 0.76- μm O₂ A-band, (middle) 1.6- μm weak CO₂ band, and (bottom) 2.06- μm strong CO₂ band focal plane arrays recorded by the OCO instrument while viewing the moon on February 28, 2008. Absorption features are clearly seen as dark bands in each frame. The inset shows the phase of the moon and approximate orientation of the OCO spectrometer field stop when these images were acquired.

critical pieces: the spectral dispersion and the instrument line shape (ILS) function of each detector element. The spectral dispersion describes the wavelength at which each detector element had its centroid response. The ILS, also commonly referred to as the spectral response function, represents the response of a single detector element to any wavelength of light incident upon that element. The ILS and dispersion parameters were validated using solar spectra collected by the instrument and compared against simultaneously collected spectra from a collocated high-resolution Fourier transform spectrometer (FTS) observing the same spectral regions.

This paper is organized as follows. Section II provides a brief overview of the OCO instrument. Section III describes the diode-laser method used to derive the spectral dispersion relationships and ILS functions for each OCO pixel. Section IV discusses the validation and refinement of the laser-based spectral calibration using collocated observations of the sun with a high-resolution FTS. Section V summarizes this paper and offers some concluding thoughts.

II. INSTRUMENT OVERVIEW

The OCO instrument was to measure sunlight reflected by the surface and atmosphere of the Earth in three narrow bands. The Oxygen-A band measured absorption by molecular oxygen near 0.76 μm , while two carbon dioxide bands, termed the weak and strong CO₂ bands, were located near 1.6 and 2.0 μm , respectively. A spectrum of the moon in all three bands taken with the flight instrument from Pasadena, CA, is shown in Fig. 1.

Manuscript received July 7, 2010; revised December 10, 2010; accepted January 16, 2011. Date of publication March 3, 2011; date of current version June 24, 2011.

J. O. Day was with the Department of Atmospheric Science, Colorado State University, Fort Collins, CO 80523-1371 USA. He is now with the Office of U.S. Senator Al Franken, Washington, DC 20510 USA.

C. W. O'Dell is with the Department of Atmospheric Science, Colorado State University, Fort Collins, CO 80523-1375 USA.

R. Pollock, C. J. Bruegge, D. Rider, D. Crisp, and C. E. Miller are with the Jet Propulsion Laboratory, California Institute of Technology, Pasadena, CA 91109 USA.

Color versions of one or more of the figures in this paper are available online at <http://ieeexplore.ieee.org>.

Digital Object Identifier 10.1109/TGRS.2011.2107745

TABLE I
SUMMARY OF OCO INSTRUMENT PERFORMANCE PARAMETERS

Parameter	Performance	Units	Comments
Spectral Ranges	0.757 - 0.772 1.590 - 1.621 2.041 - 2.082	μm	Band 1: O ₂ A-Band Band 2: weak CO ₂ Band Band 3: strong CO ₂ Band
Spectral Resolving Power	$\sim 21,000:1$	-	$\lambda/\Delta\lambda$ - varies with band and wavelength within band
Noise Equivalent Radiance (dark)	3.4×10^{-2} 4.6×10^{-3} 1.7×10^{-3}	$\text{W/m}^2/\mu\text{m/sr}$	O ₂ A-Band weak CO ₂ Band strong CO ₂ Band
Signal to Noise Ratio (5% albedo @ 60° solar zenith angle)	310:1 340:1 230:1	-	O ₂ A-Band (at 15.1 $\text{W/m}^2/\mu\text{m/sr}$) weak CO ₂ (at 2.6 $\text{W/m}^2/\mu\text{m/sr}$) strong CO ₂ (at 1.1 $\text{W/m}^2/\mu\text{m/sr}$)
IFOV	0.8×0.01	degrees	
Frame Rate	3	Hz	Integration time $\sim 98\%$ of frame time

The instrument consisted of three grating spectrometers, one for each spectral band. Light was directed into the spectrometers through a common telescope and a series of beam splitters and reimagers. Just before the incoming light enters each spectrometer, a linear polarizer selected the polarization vector parallel to the entrance slit. Each spectrometer worked in first order and used a flat holographic grating. The system was optically fast ($F/1.8$) and yielded a high signal-to-noise ratio (SNR) (typically greater than 300:1). See [5] for further details of the instrument optical design. A summary of relevant instrument parameters is shown in Table I.

At each spectrometer's focus, an area array collected the spectrum. As is typical in imaging spectrometers, one dimension measured field angles along the slit, and the other dimension measured different wavelengths. The detectors were 1024×1024 arrays. The O₂ A-band was silicon (HyViSI) Hawaii-1RG, and the two CO₂ detectors were HgCdTe Hawaii-1RG; all were manufactured by Teledyne Scientific and Imaging, LLC. The OCO detectors were cooled to 180 K (O₂ A) and 120 K (weak CO₂ and strong CO₂) and actively controlled to within ± 1 K. Only 160 pixels in the spatial dimension were used out of the 1024. Sets of 20 were averaged onboard to yield eight spatial footprints¹; each would have had a 1.5-km field of view on the ground. In the spectral dimension, four pixels were blacked out on each side of the array, leaving 1016 pixels (or channels) per band per footprint. This meant that OCO had a total of 3048 spectral channels in each of the eight separate spatial footprints.

The OCO instrument was designed to have a spectral sampling of approximately two detector elements per full width at half maximum (FWHM) in each band and a spectral resolving power $\lambda/\Delta\lambda$ of approximately 20 000, which is sufficient to resolve individual rovibrational transitions of oxygen and CO₂ from the neighboring continuum. The spectral resolving power, as well as spectral dispersion, was determined primarily by the three flat holographic diffraction gratings, one for each measured spectral band. The specific shape of the OCO ILS function was determined by the slit width, pixel pitch, optical aberrations, diffraction, detector crosstalk, and stray light in an approximate descending order of importance.

¹An onboard map of bad pixels was applied such that bad pixels were given zero weight in this average.

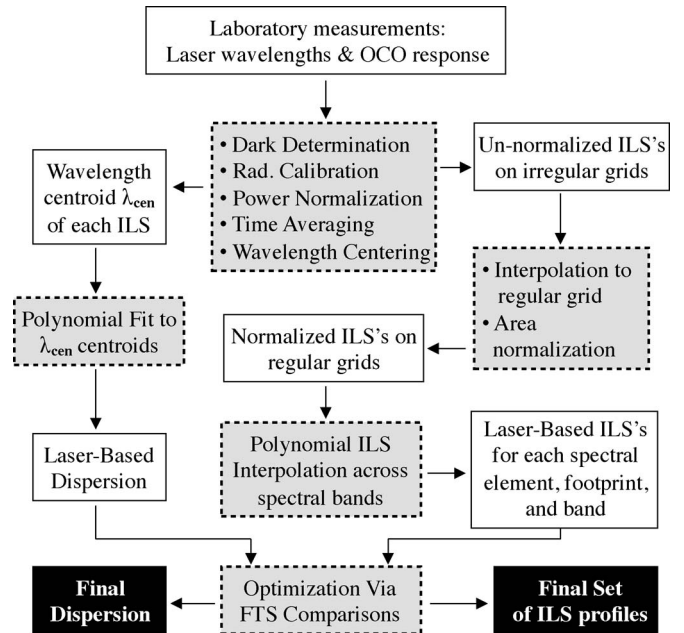


Fig. 2. Flowchart showing the basic steps in determining the instrument dispersion and ILS for each pixel. White boxes represent data sets, gray boxes represent processing steps, and black boxes represent final spectral calibration products.

III. INITIAL ILS AND DISPERSION DETERMINATION

The central challenge of the OCO spectral calibration was determining not just a single ILS, but rather the ILS for each and every spectral pixel index, footprint, and band. The three bands, eight footprints per band, and 1016 spectral pixels per footprint yield in theory 24 384 individual ILS functions. This is in contrast to, e.g., the Thermal and Near Infrared Sensor for Carbon Observations (TANSO)-FTS aboard the Greenhouse Gases Observing Satellite (GOSAT) [6], [7], which in theory has just two ILS functions (one per polarization). However, the physics of the OCO instrument design indicates that the ILS and centroid wavelength response (dispersion) of OCO should vary smoothly in the spectral dimension across each band, mitigating the challenge. The overall procedure for determining the preflight spectral calibration (i.e., spectral dispersion and ILS for each pixel) is shown in Fig. 2.

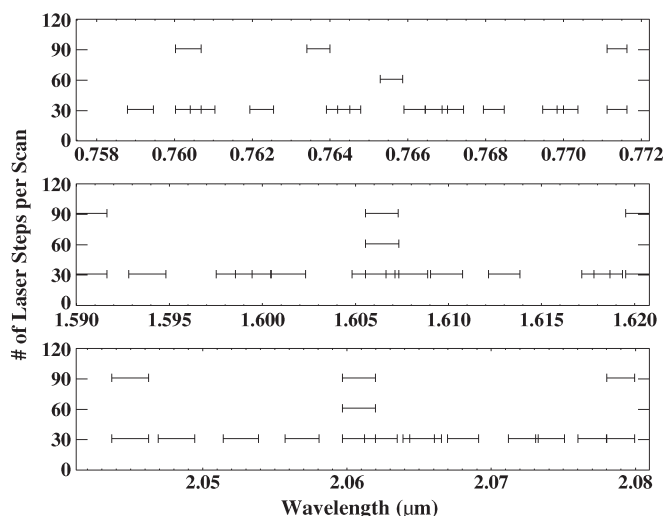


Fig. 3. Wavelength scan ranges used in the tunable diode-laser tests. There were 19 small wavelength ranges scanned for each spectral band, although there was some overlap of the scan ranges as shown. The vertical axis depicts the number of individual wavelength steps in a given scan (or sweep). From top to bottom are shown the O₂ A-band, weak CO₂ band, and strong CO₂ band.

A. Laser-Diode Test Setup

The ILS functions and spectral dispersion were determined predominantly from diode-laser experiments. These tests were conducted with three separate tunable diode lasers² having instantaneous linewidths < 1 MHz, one for each of the OCO bands. Each laser was fiber coupled to both a wavemeter³ and a 2-in-diameter integrating sphere⁴ located at the focus of a collimator. The fiber splitters for the 760- and 1560-nm bands had a 96/4 split ratio, sending 4% of the power to each wavemeter. The splitter for the 2060-nm band had a 50/50 split ratio because that wavemeter required more power. The collimator uniformly illuminated the entrance telescope of the OCO instrument. This collimated light passed into the vacuum chamber through a 6.5-in-diameter window,⁵ where it uniformly illuminated the entrance telescope of the OCO instrument.

Each tunable diode-laser test consisted of setting the lasers to a specific wavelength, waiting for frequency and intensity stabilization, averaging several seconds of data, and then scanning the laser wavelength by a small fraction of the FWHM to repeat the process. The lasers typically required tens of seconds to properly stabilize at the desired wavelength. Scanning the entire spectral range of each band in this manner would have taken many days and was impractical. Therefore, detailed ILS characterizations were performed over a limited set of wavelengths that spanned each spectral range and could be interpreted to parameterize all of the ILS functions.

Fig. 3 shows the laser scans that were used for the ILS determination. There were 19 such scans for each spectral band. Each horizontal line segment denotes a laser wavelength

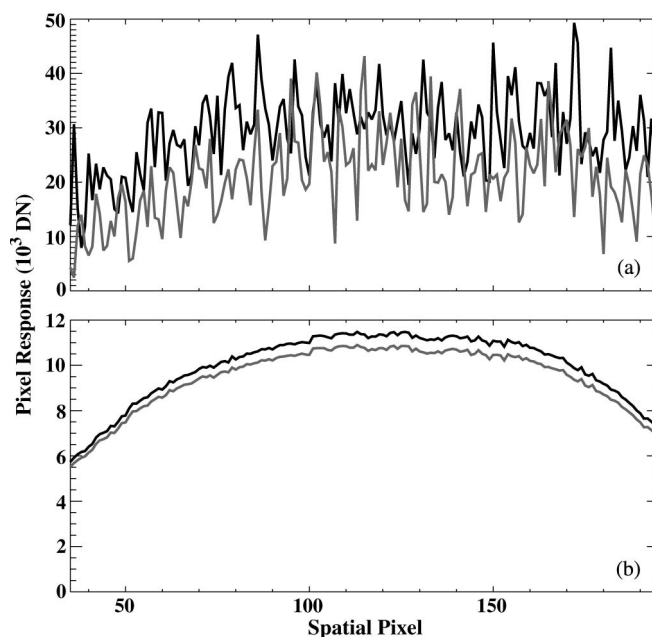


Fig. 4. Plot of dark-subtracted pixel response to diode laser along a spatial row on the 1.6- μm band focal plane array for a single spectral point near band center. These data have not been averaged down to eight spatial footprints; the full spatial resolution has been retained for clarity. Black curves are for one laser wavelength, and gray curves are for a nearby laser wavelength. Units are digital numbers (DN) or counts. (a) An early test showing large amount of speckle, manifested as a nearly random intensity at each pixel. The gray trace has been offset by 10^3 DN for clarity. (b) A later test after the spinning ground glass disk was introduced to reduce speckle. The speckle has been almost entirely eliminated, although the laser power received by the instrument has been significantly reduced.

scan range; the vertical axis shows the number of discrete wavelengths within such a scan range. A typical scan had 30 wavelengths with a step size such that there were ~ 60 laser wavelengths per ILS FWHM. Note that, since there were ~ 2 – 2.5 spectral samples per FWHM, this represents 20–30 laser steps per spectral sample. A smaller number of tests were performed with 90 wavelengths per scan to provide detailed characterization of the cores of the ILS functions.

Early laser test data were difficult to interpret due to laser speckle. Laser speckle is the random intensity pattern that results from the interference of photons with varying phases. As shown in Fig. 4(a), each time the laser wavelength was changed, the speckle pattern would also change, causing changes in the pattern of light on the focal plane that were unrelated to the instrument ILS. The data used for final determination of the ILS were collected with a spinning ground glass disk⁶ placed in front of the integrating sphere aperture. This technique minimized laser speckle by modulating the phase coherence of the laser light on a time scale that was short relative to the 3-Hz frame rate of the OCO instrument. By averaging over a few dozen frames, the speckle was almost entirely eliminated [see Fig. 4(b)]. The remaining variations in pixel response were then due to laser frequency jitter and detector noise alone. One drawback of using the spinning disk was a reduction in the laser power illuminating the instrument by a factor of approximately

²New Focus, Velocity 6300 series.

³Burleigh (EXFO) model WA-1000.

⁴The sphere was manufactured by Sphere Optics with their proprietary Zenith coating.

⁵Composed of Heraeus F7410 material.

⁶The 6-in-diameter disk was made of fused silica and rotated at several hundred revolutions per minute; its surface was roughened via sandblasting.

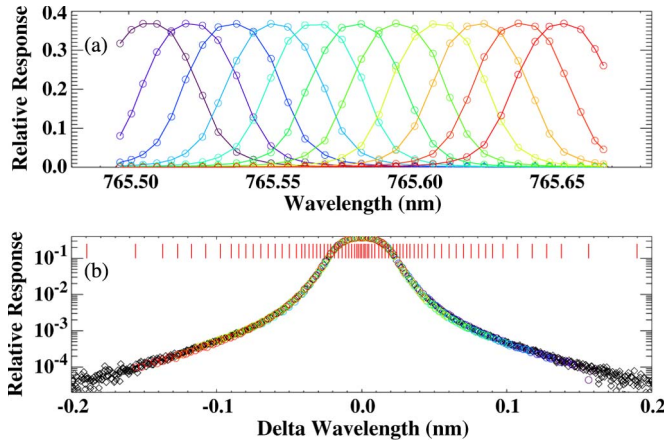


Fig. 5. Data recorded from the laser scans as seen by each of several neighboring pixels in the O_2 A-band. In panel (a), the signal from a set of 11 pixels is displayed in different colors. In panel (b), these channels are combined to give a single set of data with a much higher resolution, as shown by the colored circles. Additional pixels with smaller responses are shown as black diamonds; their wavelength centroids were approximated as described in the text. These pixels contained information on the far wings. The red vertical lines near the top of panel (b) represent the wavelength positions used to represent the ILS on a fixed wavelength grid.

three. The curved response shape evident in Fig. 4(b) was due to nonuniform optical illumination of the detectors inside the instrument (automatically accounted for in the radiometric calibration).

Laser power fluctuations added an additional level of complexity to the measurements. The laser power was found to fluctuate over both short and long time scales and therefore required precise quantification so the effect could be divided out. It was found that the laser power could be determined by simply summing the calibrated response of the flight instrument for any time sample. Once known, the power fluctuations were divided out of the signal. Finally, the signal was averaged over the period for which the laser was stabilized at a given wavelength in order to reduce instrument noise.

B. ILS Averaging and Gridding

As described in Section III-A, 19 laser scans were performed for each spectrometer band. Over each scan, several tens of pixels recorded signals clearly distinguishable from instrument noise levels. This is shown in Fig. 5(a), which shows the response of the 11 spectral pixels with the highest response to a particular laser scan; the response for each spectral pixel is shown in a different color. As expected, these 11 pixels seem to have nearly identical ILSs; this indicates that there was not a serious fringing problem, unlike the Atmospheric Infrared Sounder instrument [8], which also used a grating spectrometer. Unfortunately, there was only limited information (30 data points) gained for the ILS of an individual pixel. In order to maximize information about the ILS over a given scan range, two assumptions were made. First, the average ILS of a set of several tens of adjacent spectral pixels represented the ILS of the spectral pixel falling in the center of that set. Second, the ILS varied smoothly across the entire spectrometer band to enable representing this dependence as a polynomial (see Section III-C). Both of these assumptions were consistent with

the physics of the OCO instrument and were ultimately borne out by the success of meeting the ILS knowledge accuracy requirements (see Section IV-D).

Therefore, each laser scan would yield precisely one ILS function, taken to characterize the pixel falling in the middle of the range of instrument pixels that were probed during the scan. The separate responses of each pixel were combined by centering each pixel's response about its respective wavelength centroid. The centroid wavelength λ_{cen} of each pixel was determined with a simple Gaussian fit to the core of each ILS. We emphasize that this Gaussian fit was *only* used to determine the wavelength centroids; it was not used to characterize the ILS shapes themselves. Fig. 5(b) shows a semilog plot showing the centered response of each pixel to the laser scan as a function of $\Delta\lambda = \lambda - \lambda_{cen}$; the colors represent the different pixels from panel (a).

However, many pixels whose cores were not scanned over directly nonetheless did show nonzero response to the laser and contained valuable information about the ILS far wings. It was found that the centroid wavelengths of the central 11 pixels, determined from Gaussian fits, were well approximated locally as a linear function of spectral pixel index. Thus, the wavelength centroids of those pixels whose centers were not scanned over directly could nonetheless be well approximated via this linear relationship, and their response could therefore be included in synthesizing the average ILS function for the scan. The response of these pixels is shown as the black diamonds in Fig. 5(b). This average ILS was therefore determined with a resolution more than an order of magnitude greater than the measurements for any individual pixel. Again, this was taken to represent the average ILS of the pixels in this particular scan range.

We were unsuccessful in finding a simple functional form to the synthetic ILS data such as in Fig. 5(b). Among the functions tried were the combination of Sigmoid and Lorentzian functions, double Sigmoid, and several Chebyshev rational functions. Since none of these forms was able to meet the OCO requirements for accuracy on ILS knowledge, we created a lookup table to describe the ILS in each spectral range by interpolating the fitted ILS functions onto a predetermined $\Delta\lambda$ grid. The red vertical red lines in Fig. 5(b) represent this grid for one of the OCO bands.

The ~ 160 $\Delta\lambda$ grid points were chosen such that the grid sampling in the ILS core, where the pixel response was very sensitive to small changes in the ILS profile, was much greater than the sampling in the wings of the ILS. The interpolation was performed by fitting a cubic polynomial to the samples nearest the desired grid point. This process was repeated for all 19 laser scans for each spatial footprint and spectral band. These were then normalized such that the area under each ILS profile was unity. This process resulted in tabular ILS profiles assumed to be representative of the ILS for the pixel at the center wavelength of the corresponding laser scan.

C. ILS Spectral Variation

In order to determine the ILS profile at all 1016 pixels in an OCO spectral band, an additional step was required. As stated

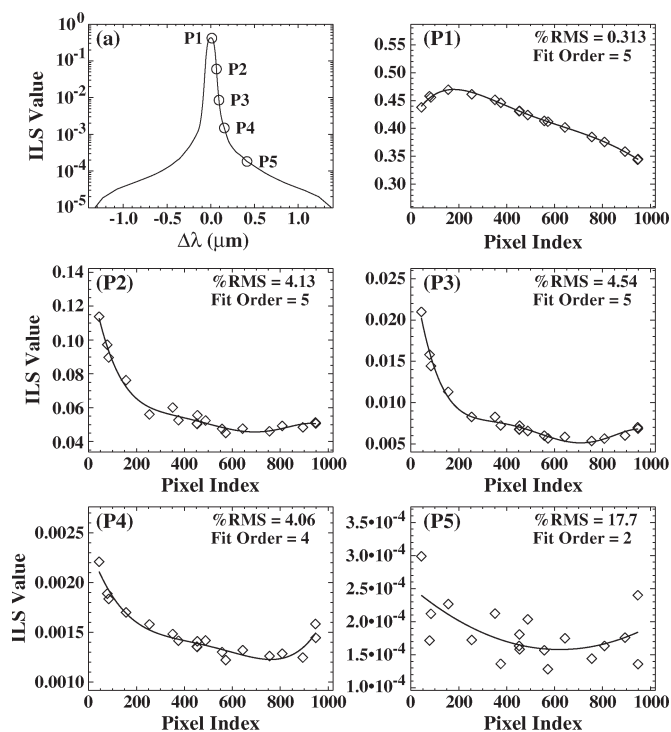


Fig. 6. Polynomial fit of the dependence of pixel relative response on spectral pixel index. Panel (a) shows the mean ILS for the strong CO_2 band, footprint 4. Panels P1–P5 show the polynomial fits of the ILS dependence on spectral pixel index for the locations P1–P5 depicted in panel (a). The fit orders and % rms values are also given. Fits from second to fifth order were used; for a given $\Delta\lambda$ grid point, the fit order was increased until there was no significant reduction in the rms residuals.

previously, it was assumed that each ILS varied smoothly as a function of λ_{cen} across each spectral band. Therefore, the final step in this process was to fit a polynomial separately to each of the ~ 160 preset $\Delta\lambda$ grid points as a function of spectral pixel index. However, it was found that the polynomial order required to make a good fit depended on where in the ILS one was fitting. In the ILS wings, a second-order fit was generally sufficient, but near the ILS core, up to a fifth-order fit was sometimes required. The lowest order polynomial that produced a reasonable fit was used for each of the grid points. Representative fits for the strong CO_2 band ILS are shown in Fig. 6. Five positions representing parts of the ILS from the core to well down into the wings are shown. It is evident that, in some locations within the ILS function, a polynomial is not necessarily the best choice for the functional form of ILS spectral variation, although it was deemed adequate.

Unfortunately, the polynomial fits tended to produce ILS profiles that were not smooth pseudo-Lorentzians at the edges of the spectrometer bands. This was because, for example, the 19 laser scans did not cover the 50 lowest wavelength pixels in the O_2 A-band which means that there was no information about the response trend of a particular grid point at that band edge. As such, the fit values were simply held constant from the last measured pixel location to the band edge.

With polynomial fits for all $\Delta\lambda$ grid points in hand, the ILS functions for each spectrometer pixel were area normalized once again. The resulting product was then an ILS function on the regular $\Delta\lambda$ grid for all 1016 pixels and eight footprints in

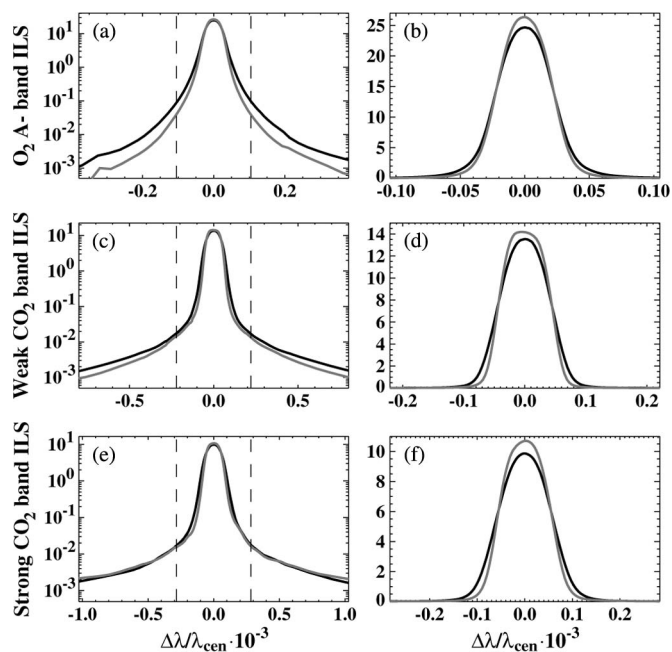


Fig. 7. Summary of the ILS profiles derived from the tunable diode-laser data. Panel (a) shows a semilog plot of the ILS for spectral pixel indexes (black) 50 and (gray) 950 for the O_2 A-band. Panel (b) shows a linear plot of the ILS core, demarcated by the dashed vertical lines in panel (a). Panels (c) and (d) are same as Panels (a) and (b) but for the weak CO_2 band. Panels (e) and (f) are same as Panels (a) and (b) but for the strong CO_2 band.

each of the three OCO bands. Fig. 7 shows the derived ILS profiles for the fourth spatial footprint near the left band edge (spectral pixel index 50, black) and right band edge (spectral pixel index 950, gray) for each of the three OCO bands. It was found that the profiles were not always perfectly symmetric, even in the ILS core; the asymmetry was worst in the weak CO_2 band footprint 1.

D. Spectral Dispersion

The Gaussian fits to the centroid wavelength response of each pixel, described in Section III-B, enabled a simple determination of the spectral dispersion for each of eight spatial footprints and three spectral bands of the OCO instrument. It was found that the centroid wavelengths of the pixels of a given footprint had a spacing that varied smoothly across the band in question and could be described by a simple polynomial. In the end, a fourth-order polynomial was sufficient to model the laser-based dispersion in all three bands. A second-order polynomial was basically sufficient in the O_2 A-band, but errors were reduced significantly by going to fourth order for the two CO_2 bands. This was particularly true in the strong CO_2 band, whose spectral dispersion was seen to have a strong third-order component.

The spectral dispersion fits and residuals are shown in Fig. 8 for footprint 4. The rms errors in the three bands are seen to be on the order of 1–2 pm and are worst in the weak CO_2 band, although for no obvious reason. These specific errors were immaterial in that the dispersion accuracy was only required via sufficient performance in comparison with the ground-based FTS spectra. This test is described in Section IV in which it

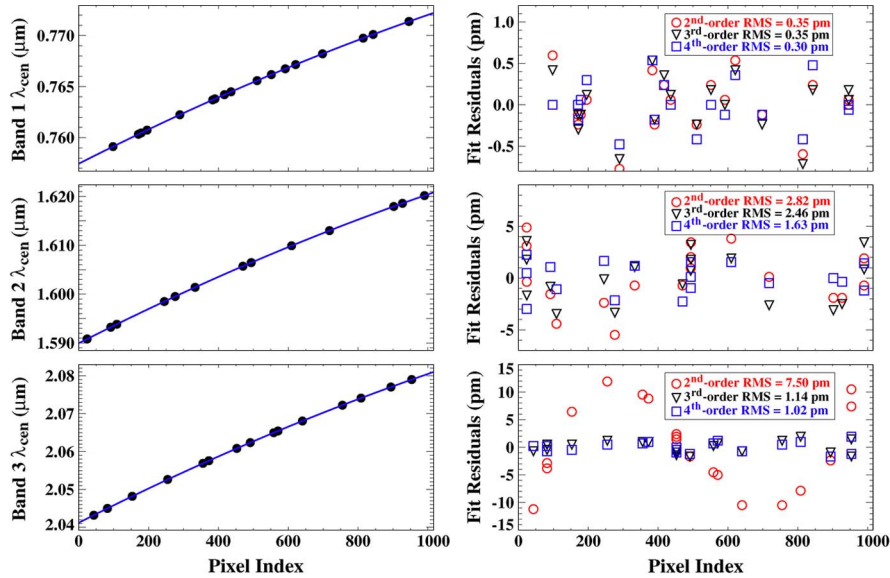


Fig. 8. Polynomial fits to spectral dispersion. (Left-hand panels) (Solid line) Fourth-order polynomial fits to footprint 4 wavelength centroids derived from (filled circles) laser data as a function of spectral pixel index (1, . . . , 1016), for the three OCO bands, respectively. Only a slight curvature is visibly apparent. (Right-hand panels) Residuals of polynomial fits to wavelength centroids of (circles) second order, (triangles) third order, and (squares) fourth order for each band. Displayed rms errors are best for the fourth-order fits, particularly for the two CO₂ bands.

will be seen that the laser-based dispersion failed to meet our prelaunch accuracy requirement and hence required refinement.

IV. REFINEMENT AND VALIDATION

A. Comparison of OCO and FTS Solar Spectra

A novel technique was employed to validate the spectral calibration of the OCO instrument. During thermal vacuum testing, there were some periods when a heliostat was used to direct sunlight into the OCO instrument aperture. Simultaneously, an FTS⁷ acquired high-resolution solar spectra. The FTS spectra provided an excellent reference standard against which to compare the calibrated OCO spectra. The FTS spectra were acquired at 0.014 cm⁻¹ unapodized resolution, which is approximately 20 times higher than the spectral resolution of the OCO instrument. Additionally, the FTS spectra had high SNR (> 10 000:1) and were characterized by a single well-determined ILS for the entire spectral range [9]. The measurements discussed here were taken at JPL on February 27, 2008.

In order to compare simultaneously acquired solar spectra from the two instruments, the FTS spectrum was convolved with the OCO instrument ILS to create a synthetic OCO-like spectrum. OCO's spectral calibration requirements necessitated agreement to within < 0.25% (rms) between the actual OCO spectra and FTS-measured synthetic spectra across all three OCO spectrometer bands. An implicit assumption with this approach was that the FTS spectra were of sufficiently higher resolution than those of OCO that they could be treated as monochromatic. This assumption was tested with independent calculations that explicitly convolved the OCO signal with

the known FTS ILS; errors associated with the assumption occurred at the 0.02% level and, thus, were deemed acceptable.

The two instruments could be expected to disagree for two reasons independent of OCO calibration accuracy. First, the integration time of the OCO instrument was 0.34 s while the FTS required 79 s to make an observation. We averaged the 237 OCO spectra taken during the FTS observation, but changes in solar zenith angle or atmospheric conditions over the 79-s period could be expected to lead to slight differences in the two sets of spectra. Second, the FTS had a smaller field of view than the OCO instrument and observed only the center of the solar disk while the OCO observed the full disk-integrated spectrum. This narrowed the observed solar lines in the synthetic spectrum, giving anomalously large relative residuals to pixels containing strong solar lines. The broadening was due to the Doppler shift of the solar absorption lines as well as the different pressure and temperature profiles at the edge of the solar disk. These were picked up by the OCO instrument but not by the FTS. For this reason, the pixels containing appreciable solar absorption features were not included in the analysis of the residual statistics.

Synthetic OCO spectra were created by convolving the simultaneously acquired FTS spectra with the ILS profiles of each OCO spectral pixel. Because the FTS spectra were radiometrically uncalibrated, an absolute comparison between the two instruments was impossible. Therefore, the spectra from both instruments were first adjusted so that their continuum levels were approximately unity. A sample FTS spectrum for the weak CO₂ band is shown in Fig. 9(a), taken when the sun was at an angle of 52.5° from the local zenith. The adjusted FTS spectrum was then convolved with the OCO ILS for each of the 1016 OCO pixels in a given band, yielding a synthetic OCO spectrum [see Fig. 9(b)]. Differencing the real and synthetic spectra yielded the residuals that were used as the basis from which to assess the accuracy of the OCO spectral calibration.

⁷Bruker IFS model 125HR.

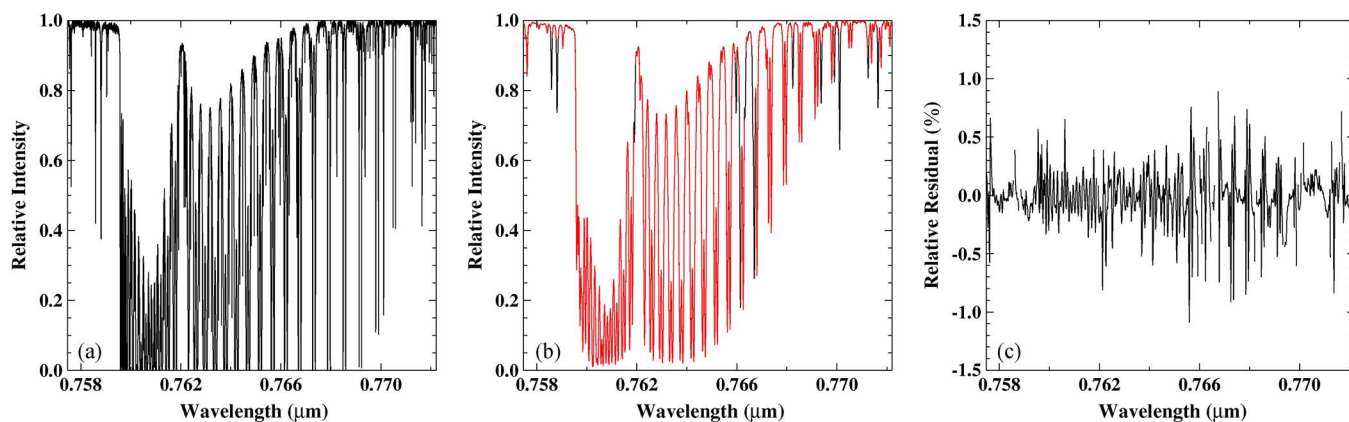


Fig. 9. Production of the synthetic spectrometer measurement. Panel (a) shows the high-resolution FTS spectrum over the weak CO₂ band. The FTS spectrum is convolved with the OCO ILS to yield a synthetic OCO-like spectrum. (Red) Synthetic spectrum is seen in panel (b) over top (black) the OCO measurement. Bad pixels and solar lines have been masked out of the synthetic spectrum. The residuals between the OCO spectrum and the synthetic spectrum are shown in panel (c).

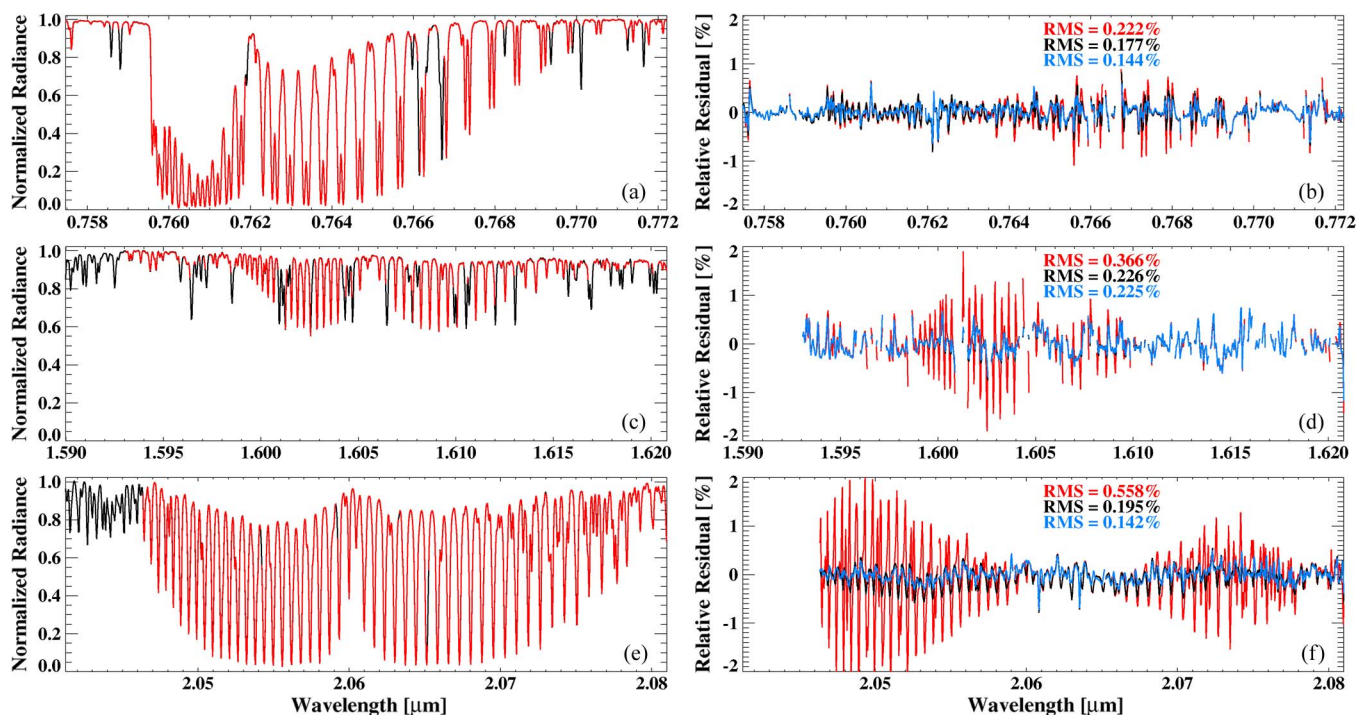


Fig. 10. Panels (a), (c), and (e) display (red) the FTS-based synthetic spectra as well as (black) the OCO spectrometer signal for the O₂ A-band, weak CO₂ band, and strong CO₂ band, respectively. Note that solar lines, bad pixels, and regions of stray light have been masked out of the synthetic spectra (the latter affects the low-wavelength end of the weak and strong CO₂ bands). Panels (b), (d), and (f) contain the relative residuals in percent for the corresponding spectrum to the left. The original laser-based ILS and dispersion equations yielded (red) residuals as high as 0.6%, greater than mission tolerances. After optimizing the dispersion parameters, the synthetic spectra produced (black) residuals that were much improved. Optimizing both the dispersion parameters and a single ILS parameter related to the level of the far wings, (blue) the residuals become better still.

Initial fits showed that imperfect parameterization of solar lines and unmasked bad OCO pixels dominated the residuals. The spectral pixels containing these features were therefore omitted from the comparisons.

B. Dispersion Refinement

Initial comparisons failed to produce rms residuals < 0.25%, even when removing bad pixels and solar lines. Therefore, we undertook an optimization process to refine the OCO spectral calibration parameters. This process is shown in Fig. 10. The left-hand panels of this plot show the measured OCO spectra

(black) and FTS-based synthetic OCO spectra (red) for all three OCO bands for spatial footprint 4. The synthetic spectra have had solar lines as well as bad pixels removed. We also omitted small portions of the two CO₂ bands that suffered from known stray light contamination. The affected regions occur at the low-wavelength end of each spectral band and also have been masked out of the synthetic OCO spectra. The right-hand panels in Fig. 10 show the residuals for the laser-based ILS and dispersion in black.

The dispersion parameters were optimized by fixing the ILS and fitting a fourth-order polynomial to the spectral dispersion until the spectral residuals were minimized. A simple

Gauss–Newton iteration approach (see, e.g., [10]) was used to perform the actual optimization. The spectral residuals resulting from the optimized dispersion parameters are plotted in black in the right-hand panels in Fig. 10. The residuals are reduced significantly in all three bands. The FTS wavelength calibration was assumed to be perfect. The refined dispersion parameters typically changed the λ_{cen} value for each OCO pixel by 1–2 pm, demonstrating the superior sensitivity of this approach as compared to the diode-laser calibration alone. The basic reason for this is because we are fitting to all atmospheric lines in the spectral band simultaneously, instead of just a few diode-laser wavelengths.

C. ILS Refinement

The ILS profiles derived from the tunable diode-laser testing were subject to potential systematic errors. For example, ILS measurements using coherent light (such as from a laser) can, under certain circumstances, yield an ILS that has a different FWHM than one determined using incoherent light [11]. Systematic errors in the OCO dark response [4] could also lead to ILS functions with incorrectly characterized wings. To account for these potential effects, two simple ILS fit parameters were adjusted in a similar manner as for the dispersion optimization. The first parameter γ simply scaled the ILS in the $\Delta\lambda$ axis by a factor of γ ; $\gamma = 1$ therefore represented no change from the laser data. The second parameter α raised the entire ILS to the power α but then rescaled the $\Delta\lambda$ axis so that the FWHM was unchanged. This had the effect of increasing ($\alpha < 1$) or decreasing ($\alpha > 1$) the relative amplitude of the ILS wings.

The ILS refinement parameters γ and α were optimized for each OCO footprint and band simultaneously with the dispersion optimization as there could be slight correlations between the two sets of parameters. It was found that γ never changed appreciably from its initial value of 1.0, meaning that the FWHM of the ILS was well measured by the laser data. However, the wing parameter α was found to be optimal at a value between 0.92 and 0.97, depending on the footprint and band, which had the effect of slightly increasing the ILS far-wing response. Residuals for the fully optimized ILS and dispersion are shown in the blue curves in Fig. 10. There is a noticeable improvement in both the O₂ A-band and strong CO₂ bands, but the weak CO₂ band residuals are virtually unchanged from those obtained using the pure laser-based ILS profiles.

D. Validation

Fig. 10 shows that adjusting both the ILS and dispersion parameters reduced the rms residuals to 0.14% for the O₂ A-band, 0.23% for the weak CO₂ band, and 0.14% for the strong CO₂ band. These residuals met the preflight spectral calibration accuracy requirements and served to validate the ILS profiles and dispersion equations. The reason for the relatively higher residuals in the weak CO₂ band is most likely weak unfiltered solar lines, but further investigation is required to confirm this.

The dispersion and ILS optimizations were performed using a single FTS spectrum taken at a solar zenith angle of 52.5°. To

test this optimized spectral calibration, comparisons of the FTS and OCO spectra were made for approximately 130 different solar spectra, taken from sunrise to midmorning on a particularly clear day and spanning solar zenith angles from 85.2° to 52°. During this test, the optical depth near the line cores varies from ~ 10 to 1.6 air masses, providing a stringent test of the refined spectral calibration. The residuals of the comparison between the OCO spectrometer and synthetic spectra changed only slightly between the beginning and end of the data set, although they did get noticeably worse for the highest solar zenith angles. However, all residuals were much better with the optimized spectral calibration as compared to the laser-based calibration, indicating that the optimized spectral calibration was general and not an artifact of the single FTS spectrum used for the optimization.

V. CONCLUSION

We have described the preflight spectral calibration of the OCO instrument, including ILS profiles and spectral dispersion, and shown that these were characterized to within the mission accuracy requirements. Accurate characterization of the ILS and dispersion was achieved by scanning single-frequency lasers across each spectral range. The spectral calibration parameters were further optimized and validated by comparing atmospheric spectra acquired simultaneously by the OCO flight instrument and a collocated high-resolution FTS. The on-orbit spectral calibration strategy was to develop a refined error model and combine this with in-flight observations to improve the ILS and dispersion equations further. In particular, observations of the solar spectrum over an entire dayside orbit would Doppler shift the solar absorption features in each band by more than two OCO spectral pixels, providing data similar to those from scanning the tunable diode lasers. These observations would have enabled the refinement and validation of the ILS and dispersion parameters in flight.

For the upcoming OCO-2 reflight, the tunable laser-diode tests will be expanded to include a larger number of more uniformly spaced wavelength scans. Also, the spinning disk will be removed, and laser speckle will be reduced by applying ultrasonic vibrations to the laser fiber. This will greatly increase the laser power illuminating the OCO-2 instrument, allowing for more accurate characterization of the ILS far wings. These data, coupled with the analysis methods described in this paper, define the basic road map for the upcoming OCO-2 spectral calibration.

ACKNOWLEDGMENT

The authors would like to thank all of the Jet Propulsion Laboratory (JPL) employees who worked tirelessly to acquire the Orbiting Carbon Observatory thermal vacuum test data. The authors would also like to thank the two anonymous reviewers for their thoughtful comments on the original manuscript. A portion of the research described in this paper was carried out at the JPL, California Institute of Technology, under a contract with the National Aeronautics and Space Administration (NASA). The Colorado State University contributions to this work were carried out under NASA contract 1280999.

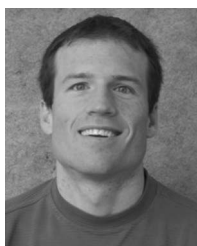
REFERENCES

- [1] D. Crisp, R. M. Atlas, F.-M. Breon, L. R. Brown, J. P. Burrows, P. Ciais, B. J. Connor, S. C. Doney, I. Y. Fung, D. J. Jacob, C. E. Miller, D. O'Brien, S. Pawson, J. T. Randerson, P. Rayner, R. J. Salawitch, S. P. Sander, B. Sen, G. L. Stephens, P. P. Tans, G. C. Toon, P. O. Wennberg, S. C. Wofsy, Y. L. Yung, Z. Kuang, B. Chudasama, G. Sprague, B. Weiss, R. Pollock, D. Kenyon, and S. Schroll, "The Orbiting Carbon Observatory (OCO) mission," *Adv. Space Res.*, vol. 34, no. 4, pp. 700–709, 2004.
- [2] D. Crisp and C. Johnson, "The Orbiting Carbon Observatory mission," *Acta Astronaut.*, vol. 56, no. 1/2, pp. 193–197, Jan. 2005.
- [3] C. E. Miller, D. Crisp, P. L. DeCola, S. C. Olsen, J. T. Randerson, A. M. Michalak, A. Alkhaled, P. Rayner, D. J. Jacob, P. Suntharalingam, D. B. A. Jones, A. S. Denning, M. E. Nicholls, S. C. Doney, S. Pawson, H. Boesch, B. J. Connor, I. Y. Fung, D. O'Brien, R. J. Salawitch, S. P. Sander, B. Sen, P. Tans, G. C. Toon, P. O. Wennberg, S. C. Wofsy, Y. L. Yung, and R. M. Law, "Precision requirements for space-based X_{CO_2} data," *J. Geophys. Res.*, vol. 112, p. D10 314, May 2007.
- [4] C. W. O'Dell, J. O. Day, C. Bruegge, R. Castano, D. Crisp, C. E. Miller, D. M. O'Brien, R. Pollock, and I. Tkatcheva, "Preflight radiometric calibration of the Orbiting Carbon Observatory," *IEEE Trans. Geosci. Remote Sens.*, 2011, to be published.
- [5] R. Haring, R. Pollock, B. Sutin, and D. Crisp, "Current development status of the Orbiting Carbon Observatory instrument optical design," in *Proc. SPIE*, M. Strojnik, Ed., 2005, vol. 5883, no. 1, p. 588 30C.
- [6] T. Hamazaki, Y. Kaneko, A. Kuze, and H. Suto, "Greenhouse gases observation from space with TANSO-FTS on GOSAT," presented at the Fourier Transform Spectroscopy/Hyperspectral Imaging Sounding Environment, Santa Fe, NM, 2007, Paper FWB1.
- [7] H. Suto, T. Kawashima, J. Yoshida, J. Ishida, A. Kuze, M. Nakajima, and T. Hamazaki, "The pre-launch performance test and calibration results of Thermal And Near-infrared Sensor for carbon Observation (TANSO) on GOSAT," in *Proc. SPIE*, R. Meynart, S. P. Neeck, H. Shimoda, and S. Habib, Eds., 2008, vol. 7106, no. 1, p. 710 60L.
- [8] L. L. Strow, S. E. Hannon, M. Weiler, K. Overoye, S. L. Gaiser, and H. H. Aumann, "Prelaunch spectral calibration of the atmospheric infrared sounder (AIRS)," *IEEE Trans. Geosci. Remote Sens.*, vol. 41, no. 2, pp. 274–286, Feb. 2003.
- [9] R. A. Washenfelder, G. C. Toon, J.-F. Blavier, Z. Yang, N. T. Allen, P. O. Wennberg, S. A. Vay, D. M. Matross, and B. C. Daube, "Carbon dioxide column abundances at the Wisconsin Tall Tower site," *J. Geophys. Res.*, vol. 111, p. D22 305, 2006.
- [10] C. D. Rodgers, *Inverse Methods for Atmospheric Sounding: Theory and Practice*. Singapore: World Scientific, 2000.
- [11] P. Mouroulis and R. O. Green, "Spectral response evaluation and computation for pushbroom imaging spectrometers," in *Proc. SPIE*, P. Z. Mouroulis, W. J. Smith, and R. B. Johnson, Eds., 2007, vol. 6667, no. 1, p. 666 70G.



Jason O. Day received the Ph.D. degree in atomic physics from the University of Wisconsin, Madison.

From 2008 to 2009, he was a Postdoctoral Fellow with the Orbiting Carbon Observatory team. He is currently an American Geophysical Union Congressional Science Fellow with the Office of U.S. Senator Al Franken.



Christopher W. O'Dell received the Ph.D. degree in physics from the University of Wisconsin, Madison, in 2001, where he studied the cosmic microwave background radiation.

After postdoctoral positions in both astronomy and microwave remote sensing, he joined the research staff with Colorado State University, Fort Collins, in 2007, where he is currently a Member of the Cooperative Institute on Research in the Atmosphere. His research concerns the remote sensing of climatically important atmospheric variables such as

water vapor and carbon dioxide.



Randy Pollock received the B.S. degree in engineering and applied science from the California Institute of Technology, Pasadena, in 1991.

He is currently an Instrument Architect for the Orbiting Carbon Observatory with the Jet Propulsion Laboratory, California Institute of Technology.



Carol J. (Kastner) Bruegge received the Ph.D. degree in optical sciences from the University of Arizona, Tucson, in 1985.

From 1988 to 2003, she was a Member of the Earth Observing System Multi-angle Imaging SpectroRadiometer team. She was a Principal Investigator of the LED Spectrometer (LSpec) automatic vicarious calibration facility and also the First International Satellite Land Surface Climatology Program Field Experiment, a ground-truth hydrology experiment conducted from 1987 to 1992. She is

currently with the Jet Propulsion Laboratory, California Institute of Technology, Pasadena, where she is a Member of the Orbiting Carbon Observatory science team.



David Rider received the Ph.D. degree in physical chemistry from Michigan State University, East Lansing.

He came to the Jet Propulsion Laboratory (JPL), California Institute of Technology, Pasadena, in 1983 after completing his Ph.D. studies at Michigan State and then postdoctoral research at Stanford University. At JPL he worked on the development of a wide variety of atmospheric remote sensing instrumentation for both planetary and Earth missions. More recently he was Instrument Scientist for the

Tropospheric Emission Spectrometer (TES) on NASA's Aura Earth Observing Spacecraft. He is currently the Instrument Scientist for the Orbiting Carbon Observatory.



David Crisp is an Atmospheric Physicist and a Senior Research Scientist at the Jet Propulsion Laboratory, California Institute of Technology, Pasadena. He was the Principal Investigator of the Earth System Science Pathfinder (ESSP) Orbiting Carbon Observatory (OCO) mission, NASA's first dedicated carbon dioxide measurement mission. He is currently serving as the Science Lead for the recently approved OCO-2 mission.



Charles E. Miller received the B.S. degree in chemistry from Duke University, Durham, NC, and the Ph.D. degree in physical chemistry from the University of California, Berkeley.

He is currently with the Earth Atmospheric Science Division, Jet Propulsion Laboratory, California Institute of Technology, Pasadena. He is currently the Deputy Project Scientist for the second Orbiting Carbon Observatory mission.